Published December 6, 2010

we demonstrate a complex regulatory system in which S1P also acts as a bone attractant in certain conditions (actually functioning as a circulation repellant) through a different cognate receptor, S1PR2. In contrast to several chemokines that have already been reported to be important for OP localization, such as CCL2 (Binder et al., 2009), CCL9 (Yang et al., 2006), CXCL1 (Onan et al., 2009), and CXCL12 (Gronthos and Zannettino, 2007), we assume that the S1P–S1PR1/S1PR2 reciprocal axes contribute to regulating the initial entry/exit of OPs across the border of BM vasculature, rather than attachment at the bone surface by itself.

Given these data, we suggest the following model for S1P-mediated localization control of OPs in bone tissues in vivo (Fig. S3). As with other tissues and organs, the S1P concentration in bone tissues is relatively low (Maeda et al., 2010), forming a substantial S1P gradient between BM tissues (parenchyma), the sinusoids, and blood vessels, which is a prerequisite for S1P chemotaxis in situ. Because S1PR1 is readily down-regulated by endocytosis in a high S1P environment, OPs in blood vessels could enter into bones by S1PR2-mediated repulsion, although S1PR2-mediated OP entry into BM has not been fully demonstrated in the present experiments. In addition, we do not assume this is the only mechanism regulating OP entry but rather consider several bone-enriched chemokines, CXCL12 chief among them (Gronthos and Zannettino, 2007), to also be involved in bone recruitment, with S1PR2-mediated chemorepulsion facilitating this process. Once they entered into the parenchyma, S1PR1 would be reexpressed on the cell surface, prompting potential reentry into the circulation if other factors (chemokines and adhesion molecules) at the bone surface do not override this chemoattractive effect. Although it cannot be measured precisely, S1P concentration in BM sinusoids, because of leakage across endothelial barriers, might be expected to be intermediate between parenchymal tissues and blood vessels. If this is the case, it is plausible that OPs can exit from bone tissue via the sinusoids, whose S1P concentration can only activate S1PR1 but not S1PR2. The concept that sinusoids are the place of OP mobilization agrees with our observation that sinusoidal cells have high motility in JTE-treated BM (Fig. S2).

This study clearly demonstrates that reciprocal actions of two S1P receptors regulate the steady-state migration propensities of OPs, constituting a versatile cycle that may play a crucial role in control of osteoclastogenesis and bone remodeling. Although therapeutics in bone-resorptive disorders have so far been targeted mature OCs (such as bisphosphonates) or late OPs fairly committed to OC differentiation (such as denosumab, i.e., anti-RANKL neutralizing antibody), treatment targeting monocytoid early OPs, such as S1P modulators, might be promising as a novel line of treatment in these disorders.

MATERIALS AND METHODS

Cell culture. RAW264.7, a mouse macrophage/monocyte lineage cell line, and mouse BM-derived M-CSF–dependent monocytes (BM-MDM), containing OP cells, were cultured as previously described (Ishii et al., 2006). To stimulate osteoclastogenesis, 50 ng/ml RANKL (PeproTech) was added to the medium and the cells were incubated for 3–4 d. In some experiments, cell were pretreated with siRNAs targeting S1PR1 or S1PR2 (ON-TARGET plus siRNA library; Thermo Fisher Scientific) using a conventional transfection reagent (Lipofectamine 2000; Invitrogen).

In vitro chemotaxis chamber assay. Chemotactic migration of cells was measured in a modified Boyden chamber as described previously (Okamoto et al., 2000).

EZ-Taxiscan chemotaxis assay. Chemotaxis experiments were also conducted in an EZ-Taxiscan chamber according to the manufacturer's protocol (Effector Cell Institute). The EZ-Taxiscan is a visually accessible chemotactic chamber, in which one compartment, containing ligand (S1P), and another compartment, containing cells, are connected by a microchannel. A stable concentration gradient of chemoattractant can be reproducibly formed and maintained through the channel without medium flow. Phase-contrast images of migrating cells were acquired at 1-min intervals. Sequential image data were processed with ImageJ (National Institutes of Health [NIH]), equipped with an add-on program, MT Track J.

Mice. C57BL/6 mice and CX_3CR1-EGFP knockin mice (Jung et al., 2000) were obtained from The Jackson Laboratory. *S1PR2*-deficient mice (Kono et al., 2004) were obtained from R.L. Proia (National Institute of Diabetes and Digestive and Kidney Diseases, NIH, Bethesda, MD). All mice were bred and maintained under specific pathogen-free conditions at animal facilities of NIH and Osaka University, and all the animal experiments were performed according to NIH institutional guidelines and Osaka University animal experimental guidelines under approved protocols. Mutant mice were genotyped by PCR. All mice were housed and handled according to the institutional guidelines under approved protocols.

Two-photon intravital bone tissue imaging. Intravital microscopy of mouse calvaria bone tissues was performed using a protocol modified from a previous study (Ishii et al., 2009). Mice were anesthetized with isoflurane (Escain; 2.5% vaporized in an 80:20 mixture of O_2 and air), and the hair in the neck and scalp was removed with hair removal lotion (Epilat). The frontoparietal skull was exposed and the mouse head was immobilized in a custom-made stereotactic holder. A catheter was placed into the tail vein with a 30-gauge needle attached to PE-10 tubing (BD). The imaging system was composed of a multiphoton microscope (SP5; Leica) driven by a laser (MaiTai HP Ti:Sapphire; Spectraphysics) tuned to 880 nm and an upright microscope (DM6000B; Leica) equipped with a 20× water immersion objective (HCX APO, N.A. 1.0; Leica). The microscope was enclosed in an environmental chamber in which anesthetized mice were warmed by heated air. Fluorescent cells were detected through a bandpass emission filter at 525/50 nm (for EGFP). Vessels were visualized by injecting 70 kD of Texas red–conjugated dextran (detected using a 650/50 nm filter) i.v. immediately before imaging. In some experiments, 3 mg/kg JTE013 (Tocris Bioscience) dissolved in a vehicle (PBS containing 5% acidified DMSO and 3% fatty acid–free BSA) or vehicle only was injected during the imaging. Image stacks were collected at a 3-μm vertical step size at a depth of 100–150 μm below the skull bone surface. For 3D videos, four sequential image stacks were acquired at 3-μm z spacing to cover a volume of 154 μm × 154 μm × 9.0 μm. The time resolution was 1 min. Raw imaging data were processed with Imaris (Bitplane) with a Gaussian filter for noise reduction. Automatic 3D object tracking with Imaris Spots was aided with manual corrections to retrieve cell spatial coordinates over time.

Mouse treatment experiment. Nine 8-wk-old female, wild-type, or S1PR2$^{-/-}$ mice were injected i.p. with PBS, 2 mg/kg GST-RANKL dissolved in PBS (Tomimori et al., 2009), and 2 mg/kg GST-RANKL and 3 mg/kg JTE013 (dissolved in PBS containing 5% acidified DMSO and 3% fatty acid–free BSA) for 2 d. The mice were then sacrificed and femurs were excised and subjected to histomorphometrical analyses.

Histomorphometry of bone tissues. Trabecular bone morphometry within the metaphyseal region of distal femur was quantified using micro-CT

Published December 6, 2010

JEM

(ScanXmate-RX; Comscantechno Inc.). 3D microstructural image data were reconstructed, and structural indices, such as B.V./T.V., Tb.Th., and Tb.N., were calculated using TRI/3D-BON software (RATOC Systems). Bone morphometric analysis was performed as previously described (Parfitt et al., 1987).

Flow cytometry. All reagents were purchased from BD. To examine the composition of peripheral blood mononuclear cells, blood was collected from the retroorbital plexus with a heparinized glass pipette from mice treated i.p. 2 h previously with 3 mg/kg JTE013 or vehicle. After removing the red blood cells by ACK lysis buffer (Invitrogen), cells were stained with FITC-conjugated anti-CD11b and PE-Cy7–conjugated anti-CD3, using conventional methods. Flow cytometric data were collected on a FACSCanto II (BD) and analyzed with FlowJo software (Tree Star, Inc.).

Statistics. The Mann-Whitney rank sum test was used to calculate p-values for highly skewed distributions. For Gaussian-like distributions, two-tailed Student's *t* tests were used.

Online supplemental material. Fig. S1 shows chemotaxis and in vitro osteoclastogenesis of S1PR2 knockout OPs. Fig. S2 shows in vivo S1PR2-mediated migration control of CX_3CR1^+ OP monocytes visualized using intravital two-photon imaging. Fig. S3 shows the therapeutic effect of S1PR2 antagonist JTE013 on ovariectomy-induced osteoporosis and schematic model for S1P-mediated localization control of OPs in bone tissues. Videos 1–6 show in vitro chemotaxis of RAW264.7 cells toward an S1P gradient detected using the EZ-Taxiscan device. Videos 7 and 8 show intravital two-photon imaging of mouse skull bone tissues of CX_3CR1-EGFP hetero knockin mice. Video 9 shows intravital two-photon imaging (broad visual field) of mouse skull bone tissues of CX_3CR1-EGFP heterozygous knockin mice. Online supplemental material is available at http://www.jem.org/cgi/content/full/jem.20101474/DC1.

We thank Dr. Richard L. Proia (National Institute of Diabetes and Digestive and Kidney Diseases, National Institutes of Health [NIH]) for S1PR2-deficient mice.

This work was supported in part by the Intramural Research Program of the National Institute of Allergy and Infectious Diseases, NIH, United States Department of Health and Human Services (R.N. Germain), by grants from the International Human Frontier Science Program (LT-00387/2006-L and CDA-00059/2009; to M. Ishii), by a Grants-in-Aid for Encouragement of Young Scientists (A; 22689030), for Scientific Research on Innovative Areas (22113007; to M. Ishii), and a Funding Program for World-Leading Innovative R&D on Science and Technology (FIRST Program) from the Ministry of Education, Science, Sports and Culture of Japan, by Grants-in-Aid for Research on Allergic Disease and Immunology (H21-010; to M. Ishii) from the Ministry of Health, Labor and Welfare of Japan, and by Grants from Takeda Science Foundation (to M. Ishii), from Japan Research Foundation for Clinical Pharmacology (to M. Ishii), from Senri Lifescience Foundation (to M. Ishii), and from Mochida Memorial Foundation for Medical and Pharmaceutical Research (to M. Ishii).

The authors declare no competing financial interests.

Submitted: 22 July 2010
Accepted: 10 November 2010

REFERENCES

Binder, N.B., B. Niederreiter, O. Hoffmann, R. Stange, T. Pap, T.M. Stulnig, M. Mack, R.G. Erben, J.S. Smolen, and K. Redlich. 2009. Estrogen-dependent and C-C chemokine receptor-2-dependent pathways determine osteoclast behavior in osteoporosis. *Nat. Med.* 15:417–424. doi:10.1038/nm.1945

Gronthos, S., and A.C. Zannettino. 2007. The role of the chemokine CXCL12 in osteoclastogenesis. *Trends Endocrinol. Metab.* 18:108–113. doi:10.1016/j.tem.2007.02.002

Ishii, M., K. Iwai, M. Koike, S. Ohshima, E. Kudo-Tanaka, T. Ishii, T. Mima, Y. Katada, K. Miyatake, Y. Uchiyama, and Y. Saeki. 2006. RANKL-induced expression of tetraspanin CD9 in lipid raft membrane microdomain is essential for cell fusion during osteoclastogenesis. *J. Bone Miner. Res.* 21:965–976. doi:10.1359/jbmr.060308

Ishii, M., J.G. Egen, F. Klauschen, M. Meier-Schellersheim, Y. Saeki, J. Vacher, R.L. Proia, and R.N. Germain. 2009. Sphingosine-1-phosphate mobilizes osteoclast precursors and regulates bone homeostasis. *Nature.* 458:524–528. doi:10.1038/nature07713

Jung, S., J. Aliberti, P. Graemmel, M.J. Sunshine, G.W. Kreutzberg, A. Sher, and D.R. Littman. 2000. Analysis of fractalkine receptor CX_3CR1 function by targeted deletion and green fluorescent protein reporter gene insertion. *Mol. Cell. Biol.* 20:4106–4114. doi:10.1128/MCB.20.11.4106-4114.2000

Karsenty, G., and E.F. Wagner. 2002. Reaching a genetic and molecular understanding of skeletal development. *Dev. Cell.* 2:389–406. doi:10.1016/S1534-5807(02)00157-0

Klauschen, F., M. Ishii, H. Qi, M. Bajénoff, J.G. Egen, R.N. Germain, and M. Meier-Schellersheim. 2009. Quantifying cellular interaction dynamics in 3D fluorescence microscopy data. *Nat. Protoc.* 4:1305–1311. doi:10.1038/nprot.2009.129

Kono, M., Y. Mi, Y. Liu, T. Sasaki, M.L. Allende, Y.P. Wu, T. Yamashita, and R.L. Proia. 2004. The sphingosine-1-phosphate receptors S1P1, S1P2, and S1P3 function coordinately during embryonic angiogenesis. *J. Biol. Chem.* 279:29367–29373. doi:10.1074/jbc.M403937200

Maeda, Y., N. Seki, N. Sato, K. Sugahara, and K. Chiba. 2010. Sphingosine 1-phosphate receptor type 1 regulates egress of mature T cells from mouse bone marrow. *Int. Immunol.* 22:515–525. doi:10.1093/intimm/dxq036

Mazo, I.B., M. Honczarenko, H. Leung, L.L. Cavanagh, R. Bonasio, W. Weninger, K. Engelke, L. Xia, R.P. McEver, P.A. Koni, et al. 2005. Bone marrow is a major reservoir and site of recruitment for central memory $CD8^+$ T cells. *Immunity.* 22:259–270. doi:10.1016/j.immuni.2005.01.008

Niess, J.H., S. Brand, X. Gu, L. Landsman, S. Jung, B.A. McCormick, J.M. Vyas, M. Boes, H.L. Ploegh, J.G. Fox, et al. 2005. CX_3CR1-mediated dendritic cell access to the intestinal lumen and bacterial clearance. *Science.* 307:254–258. doi:10.1126/science.1102901

Okamoto, H., N. Takuwa, T. Yokomizo, N. Sugimoto, S. Sakurada, H. Shigematsu, and Y. Takuwa. 2000. Inhibitory regulation of Rac activation, membrane ruffling, and cell migration by the G protein-coupled sphingosine-1-phosphate receptor EDG5 but not EDG1 or EDG3. *Mol. Cell. Biol.* 20:9247–9261. doi:10.1128/MCB.20.24.9247-9261.2000

Onan, D., E.H. Allan, J.M. Quinn, J.H. Gooi, S. Pompolo, N.A. Sims, M.T. Gillespie, and T.J. Martin. 2009. The chemokine Cxcl1 is a novel target gene of parathyroid hormone (PTH)/PTH-related protein in committed osteoblasts. *Endocrinology.* 150:2244–2253. doi:10.1210/en.2008-1597

Osada, M., Y. Yatomi, T. Ohmori, H. Ikeda, and Y. Ozaki. 2002. Enhancement of sphingosine 1-phosphate-induced migration of vascular endothelial cells and smooth muscle cells by an EDG-5 antagonist. *Biochem. Biophys. Res. Commun.* 299:483–487. doi:10.1016/S0006-291X(02)02671-2

Parfitt, A.M., M.K. Drezner, F.H. Glorieux, J.A. Kanis, H. Malluche, P.J. Meunier, S.M. Ott, and R.R. Recker; Report of the ASBMR Histomorphometry Nomenclature Committee. 1987. Bone histomorphometry: standardization of nomenclature, symbols, and units. *J. Bone Miner. Res.* 2:595–610. doi:10.1002/jbmr.5650020617

Rosen, H., and E.J. Goetzl. 2005. Sphingosine 1-phosphate and its receptors: an autocrine and paracrine network. *Nat. Rev. Immunol.* 5:560–570. doi:10.1038/nri1650

Takuwa, Y. 2002. Subtype-specific differential regulation of Rho family G proteins and cell migration by the Edg family sphingosine-1-phosphate receptors. *Biochim. Biophys. Acta.* 1582:112–120.

Teitelbaum, S.L. 2000. Bone resorption by osteoclasts. *Science.* 289:1504–1508. doi:10.1126/science.289.5484.1504

Teitelbaum, S.L., and F.P. Ross. 2003. Genetic regulation of osteoclast development and function. *Nat. Rev. Genet.* 4:638–649. doi:10.1038/nrg1122

Tomimori, Y., K. Mori, M. Koide, Y. Nakamichi, T. Ninomiya, N. Udagawa, and H. Yasuda. 2009. Evaluation of pharmaceuticals with a novel 50-hour animal model of bone loss. *J. Bone Miner. Res.* 24:1194–1205. doi:10.1359/jbmr.090217

Yang, M., G. Mailhot, C.A. MacKay, A. Mason-Savas, J. Aubin, and P.R. Odgren. 2006. Chemokine and chemokine receptor expression during colony stimulating factor-1-induced osteoclast differentiation in the toothless osteopetrotic rat: a key role for CCL9 (MIP-1γ) in osteoclastogenesis in vivo and in vitro. *Blood.* 107:2262–2270. doi:10.1182/blood-2005-08-3365

Published December 6, 2010

JEM

SUPPLEMENTAL MATERIAL

Ishii et al., http://www.jem.org/cgi/content/full/jem.20101474/DC1

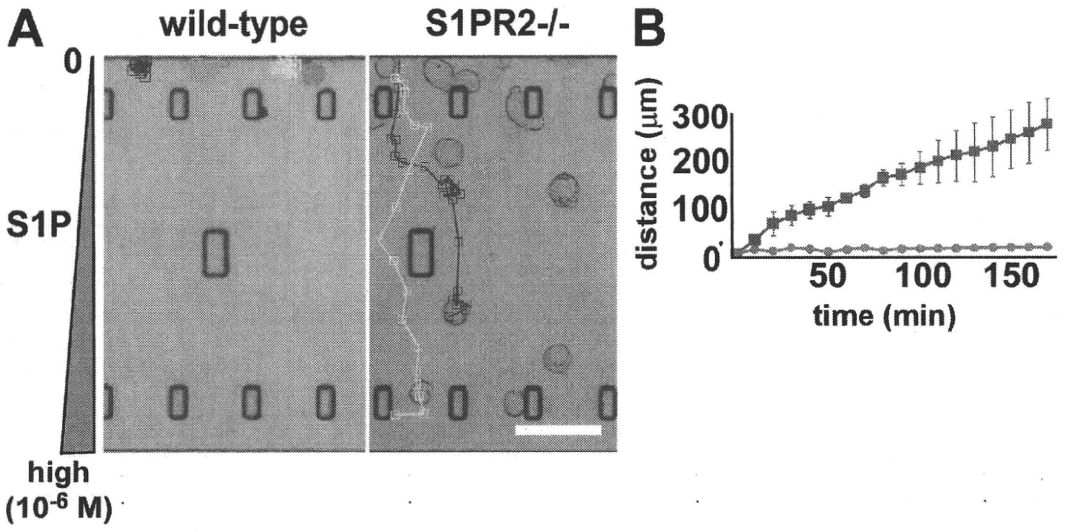

Figure S1. Chemotaxis and in vitro osteoclastogenesis of S1PR2 knockout OPs. (A) In vitro S1P-directed chemotaxis of BM-MDM OPs isolated from wild-type and S1PR2$^{-/-}$ mice. Cells were loaded onto the chamber corresponding to top of the figure, and the chamber corresponding to the bottom of the figure was filled with medium containing a high concentration of S1P (10^{-9} M). Bar, 100 μm. (B) Migration of tracked wild-type (red) and S1PR2$^{-/-}$ (blue) cells. The experiments were independently performed three times and the data were largely consistent. Each dot represents the mean value of five independent cells and error bars represent SD. (C) In vitro osteoclastogenesis from wild-type and S1PR2$^{-/-}$ BM cells. Representative images of OC-like cells differentiated from primary OPs cultured for 4 d with 100 ng/ml RANKL from wild-type (left) or S1PR2$^{-/-}$ (right) BM. Bar, 50 μm. The numbers of nuclei within TRAP-positive multinucleated (more than four nuclei) cells per visual field are 230 ± 58 (mean ± SD, wild-type) and 206 ± 73 (S1PR2$^{-/-}$), respectively (n = 5 for each). More than 1,000 nuclei were counted from three independent experiments.

Published December 6, 2010

JEM

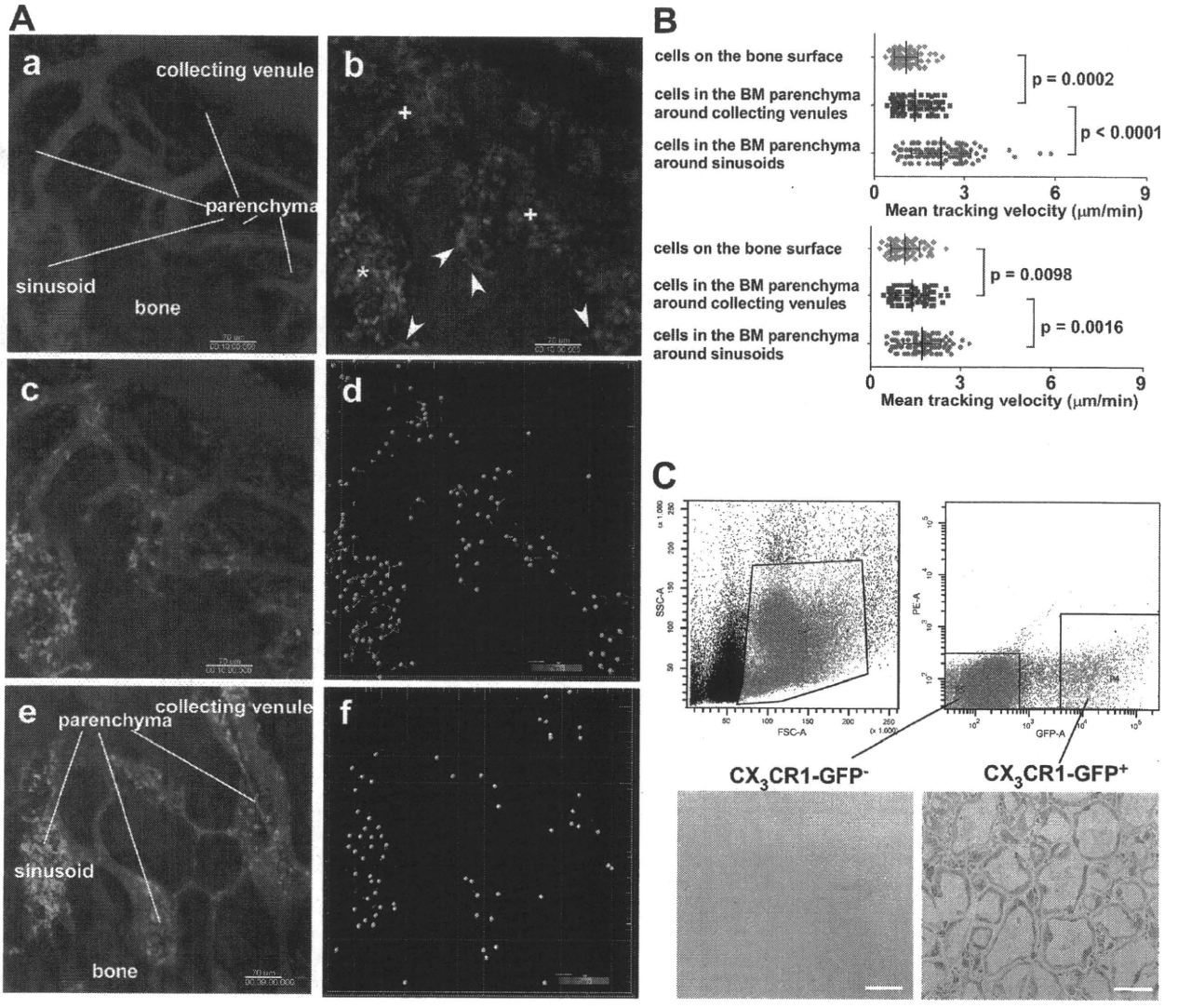

Figure S2. In vivo S1PR2-mediated migration control of OP monocytes visualized using intravital two-photon imaging. (A) Intravital two-photon imaging of mouse skull bone tissues of heterozygous CX_3CR1-EGFP knockin mice, in the presence of 3 mg/kg of the S1PR2 antagonist JTE013. (a) Basic structure of the BM cavity. Bone matrices were visualized by second harmonic generation (blue), and the microvasculature was visualized by intravenous injection of 70 kD dextran-conjugated Texas red (red). Around BM sinusoids, dextrans enter the parenchyma because of endothelial barrier leakage. (b) CX_3CR1-EGFP–positive cells, including OP cells, appear green. Arrowheads, plus signs, and asterisks represent cells on the bone surface, cells in the BM parenchyma around collecting venules, and cells in the BM parenchyma around sinusoids, respectively. (c) Triple exposures of bone (blue), vessels (red), and CX_3CR1-EGFP–positive cells (green). The movements of CX3CR1-EGFP–positive cells were tracked for 20 min (Video 9). (d) Gray spheres represent cells and colored lines show the associated trajectories. (e and f) A similar visual field of CX_3CR1-EGFP knockin mice in control condition. Triple exposure (CX_3CR1-EGFP$^+$ cells, bone and vessels; e), and trajectories of EGFP$^+$ cells (f). Bars, 70 μm. (B) Summary of mean velocity of JTE-treated (top) and control (bottom) CX_3CR1-EGFP–positive cells residing in the indicated regions of the BM cavity. Cells on the bone surface (within 10 μm from bone surface), in parenchyma around collecting venules (within 30 μm from collecting venules), and in parenchyma around sinusoids (within 30 μm of sinusoids) are represented as green diamonds, blue squares, and red circles, respectively. Data points (n = 69 for bone surface, n = 76 for parenchyma around collecting vessels, and n = 96 for sinusoidal parenchyma [top]; n = 62 for bone surface, n = 62 for parenchyma around collecting vessels, and n = 86 for sinusoidal parenchyma [bottom]) represent individual cells compiled from three independent experiments, and error bars represent SD. (C) In vitro differentiation of CX_3CR1-EGFP cells into OC-like cells. EGFP$^+$ and EGFP$^-$ cells were sorted by FACSAria (BD) and cultured in the presence of 100 ng/ml of recombinant RANKL. Bars, 100 μm.

Published December 6, 2010

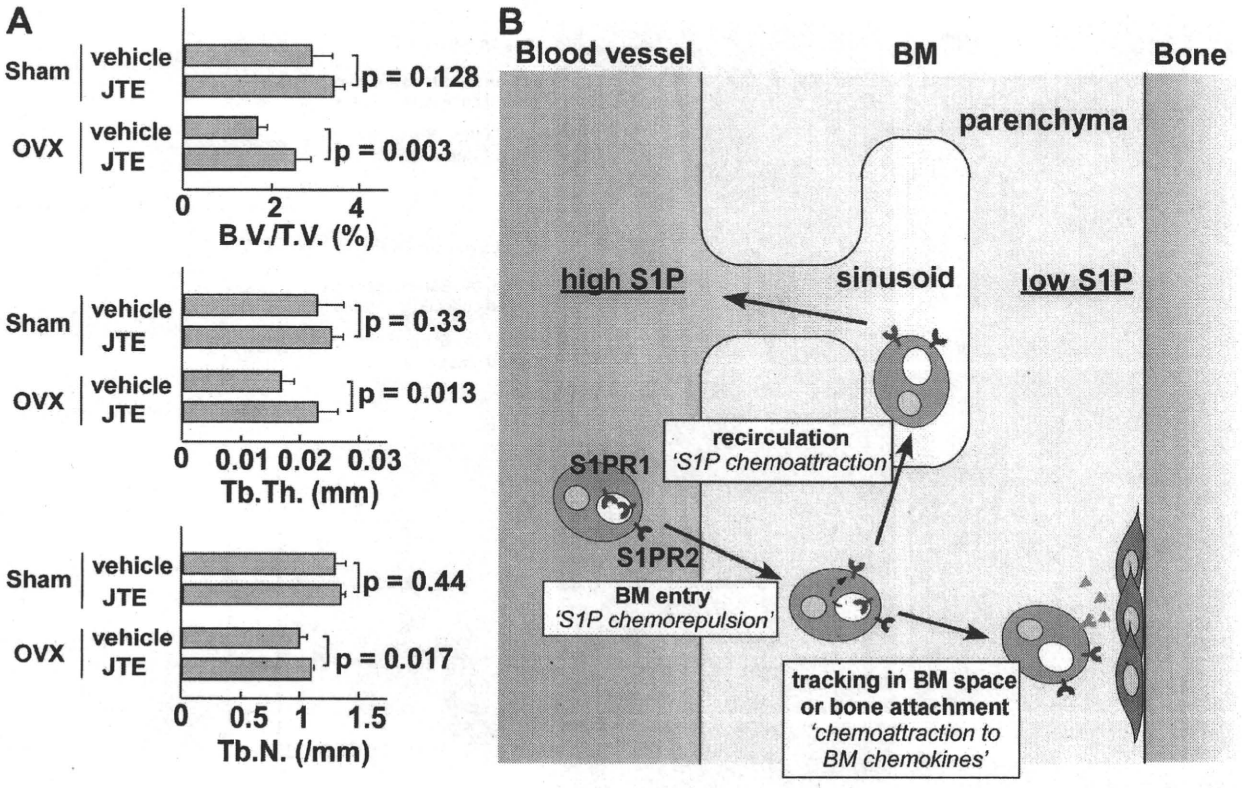

Figure S3. Therapeutic effect of S1PR2 antagonist JTE013 on ovariectomy-induced osteoporosis and schematic model for S1P-mediated localization control of OPs in bone tissues. (A) Femurs were collected from mice after four different treatments: sham operated/vehicle treated, sham operated/JTE013 treated, ovariectomized/vehicle treated, and ovariectomized/JTE013 treated. JTE013 was dissolved in PBS containing 5% acidified DMSO and 3% fatty acid–free BSA (vehicle). Mice were injected i.p. either with JTE in vehicle or with vehicle only, every day for 4 wk. Bone samples were analyzed by cone-beam μCT. Summary of the data of bone matrix density (a; bone volume/tissue volume = B.V./T.V.), trabecular thickness (b; Tb.Th.), and trabecular density (c; Tb.N.). Data represent means acquired from five independent mice and error bars represent SD. (B) Schematic model for S1P-mediated localization control of OPs in bone tissues. A substantial S1P concentration gradient is considered to be formed among BM tissues (parenchyma), sinusoid, and blood vessels, which is a prerequisite for S1P chemotaxis in situ. OP entry from blood vessels (S1P high condition) to bone parenchyma would be facilitated by chemorepulsion mediated by S1PR2 signaling. Once in the parenchyma, OPs can either migrate deeper and attach to bone surface, attracted by BM-enriched chemokines, or recirculate into blood, possibly via BM sinusoids (low or medium S1P concentration) as a result of S1PR1 signaling.

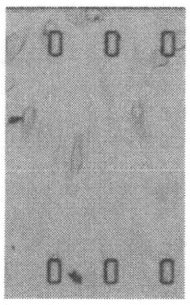

Video 1. In vitro chemotaxis of RAW264.7 cells toward an S1P gradient detected using the EZ-Taxiscan device. Cells were loaded in one side of the chamber and the other side was filled with medium containing various concentration of S1P (10^{-9} M, left). Images were taken every minute for 2 h. Playback speed is 300x.

Published December 6, 2010

JEM

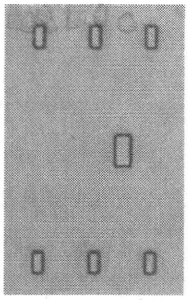

Video 2. In vitro chemotaxis of RAW264.7 cells toward an S1P gradient detected using the EZ-Taxiscan device. Cells were loaded in one side of the chamber and the other side was filled with medium containing various concentration of S1P (10^{-7} M, middle). Images were taken every minute for 2 h. Playback speed is 300×.

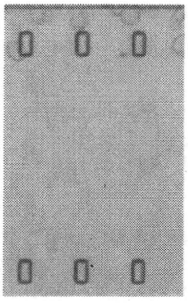

Video 3. In vitro chemotaxis of RAW264.7 cells toward an S1P gradient detected using the EZ-Taxiscan device. Cells were loaded in one side of the chamber and the other side was filled with medium containing various concentration of S1P (10^{-6} M, right). Images were taken every minute for 2 h. Playback speed is 300×.

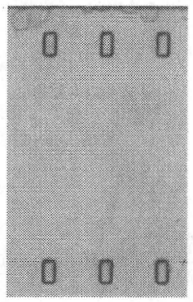

Video 4. In vitro chemotaxis of RAW264.7 cells toward an S1P gradient detected using the EZ-Taxiscan device. Cells pretreated with control RNA duplex were loaded in one side of the chamber and the other side was filled with medium containing a high concentration of S1P (10^{-6} M). Images were taken every minute for 2 h. Playback speed is 300×.

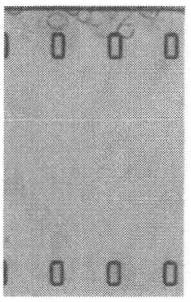

Video 5. In vitro chemotaxis of RAW264.7 cells toward an S1P gradient detected using the EZ-Taxiscan device. Cells pretreated with siRNA against S1PR1 were loaded in one side of the chamber and the other side was filled with medium containing a high concentration of S1P (10^{-6} M). Images were taken every minute for 2 h. Playback speed is 300×.

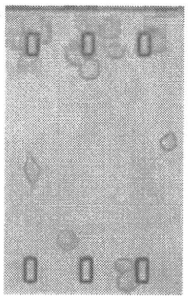

Video 6. In vitro chemotaxis of RAW264.7 cells toward an S1P gradient detected using the EZ-Taxiscan device. Cells pretreated with siRNA against S1PR2 were loaded in one side of the chamber and the other side was filled with medium containing a high concentration of S1P (10^{-6} M). Images were taken every minute for 2 h. Playback speed is 300×.

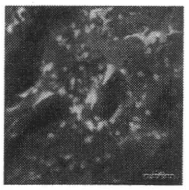

Video 7. Intravital two-photon imaging of mouse skull bone tissues of CX_3CR1-EGFP hetero knockin mice. Sequential images in the same visual field were acquired before intravenous injection of 3 mg/kg of the potent S1PR2 antagonist JTE013. CX_3CR1-EGFP–positive cells can be seen in green and the microvasculature of BM tissues was visualized by intravenous injection of 70 kD dextran-conjugated Texas red (red). Bars, 50 µm. Playback speed is 600×.

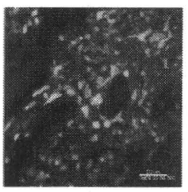

Video 8. Intravital two-photon imaging of mouse skull bone tissues of CX_3CR1-EGFP hetero knockin mice. Sequential images in the same visual field were acquired 2 h after intravenous injection of 3 mg/kg of the potent S1PR2 antagonist JTE013. CX_3CR1-EGFP–positive cells can be seen in green and the microvasculature of BM tissues was visualized by intravenous injection of 70 kD dextran-conjugated Texas red (red). Bars, 50 µm. Playback speed is 600×.

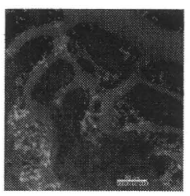

Video 9. Intravital two-photon imaging (broad visual field) of mouse skull bone tissues of CX_3CR1-EGFP heterozygous knockin mice. 2 h after intravenous injection of 3 mg/kg of the potent S1PR2 antagonist JTE013, CX_3CR1-EGFP–positive cells, microvasculature (visualized by intravenous injection of 70 kD dextran-conjugated Texas red), and bone matrices (visualized using second harmonic imaging) were seen as green, red, and blue, respectively. Bars, 70 µm. Playback speed is 600×.

Rheumatol Int
DOI 10.1007/s00296-010-1634-8

SHORT COMMUNICATION

S1P-targeted therapy for elderly rheumatoid arthritis patients with osteoporosis

Junichi Kikuta · Kaori Iwai · Yukihiko Saeki · Masaru Ishii

Received: 26 April 2010 / Accepted: 14 November 2010

Abstract Therapeutics targeting sphingosine-1-phosphate (S1P), a kind of lipid mediator regulating immune cell trafficking, has been emerging rapidly as a novel line of regimen for autoimmune diseases, including rheumatoid arthritis (RA). Here, we propose that S1P-targeted therapy is beneficial not only for limiting inflammation but for preventing bone-resorptive disorders, such as osteoporosis, by controlling the migratory behavior of osteoclast precursors and therefore would be good for treating elderly female RA patients who suffer from postmenopausal osteoporosis and arthritis simultaneously.

Keywords Rheumatoid arthritis · Osteoporosis · Sphingosine-1-phosphate

The emergence of biological agents has undoubtedly caused a paradigm shift in the treatment of rheumatoid arthritis (RA). We rheumatologists are now ambitiously aiming at a 'cure', and not just the 'care', of RA patients and have succeeded in many cases [1]. Despite the brilliant victory over this intractable disease, there are still a large number of underprivileged patients who cannot share in these advances. Elderly RA patients are the main group; many of them cannot receive biological agents due to the high frequency of occurrence of life-threatening infections. Instead, they are treated with less efficacious disease-modifying antirheumatic drugs (DMARDs) and corticosteroids. Oral corticosteroids are still commonly used in clinical practice to relieve inflammation, but this can lead to systemic dysfunction because of the progressive joint damage, which is complicated by severe osteoporosis that increases the vulnerability to fractures of the spine and femur. Recent findings provide such patients with a ray of hope.

Sphingosine-1-phosphate (S1P), a lipid mediator enriched in blood, is a critical regulator of the migration and localization of various cell types, including immune cells [2]. Extensive studies have demonstrated that lymphocytes express $S1P_1$/Edg-1, a cognate receptor for S1P, which is responsible for their recirculation from lymphoid tissues to the systemic circulation [3]. S1P attracted lot of attention from rheumatologists when FTY720 (Fingolimod), a substance isolated from a Chinese herb and long known to have immunomodulating activity, was shown to be an S1P receptor agonist [4]. Although the detailed mechanism remains elusive, FTY720 acts as an S1P receptor agonist when metabolized and is now emerging as a promising novel immunosuppressive drug that presumably acts by limiting effector lymphocyte egress from lymph nodes. FTY720 is currently being tested clinically in autoimmune diseases such as multiple sclerosis [5], and many other S1P-targeted drugs (S1P receptor agonists or S1P lyase inhibitor) are beginning to be evaluated [6].

Recently, we have demonstrated that S1P was also important for controlling the migration of osteoclasts and their precursors [7]. Using an elaborate intravital two-photon microscopy imaging technique, the migratory behavior of osteoclast precursors in live bone tissues was shown to be critically regulated by S1P, and the intravenous application of an S1P receptor agonist rapidly promoted their exit from bone into blood [8]. It was also

J. Kikuta · K. Iwai · Y. Saeki · M. Ishii
Department of Rheumatology and Clinical Research, National Osaka-Minami Medical Center, Osaka, Japan

J. Kikuta · M. Ishii (✉)
Laboratory of Biological Imaging, WPI-Immunology Frontier Research Center, Osaka University, 3-1 Yamada-oka, Osaka, Suita 565-0871, Japan
e-mail: mishii@ifrec.osaka-u.ac.jp

Published online: 28 November 2010

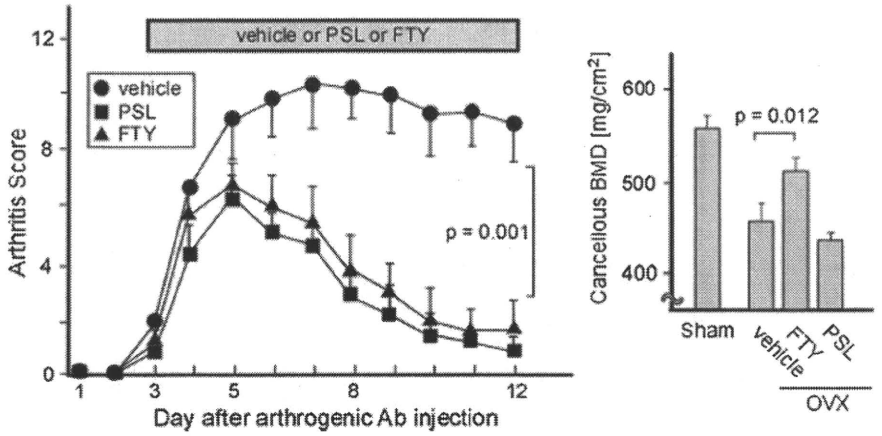

Fig. 1 The therapeutic effects of prednisolone (PSL) and FTY720 (FTY) in mice with both arthritis and osteoporosis. First, 8-week-old ovariectomized mice were injected with 5 mg of an arthrogenic anti-collagen II antibodies cocktail (Chondrex, Redmond, WA) at day 0, and then with 50 μg of lipopolysaccharide (LPS) (0111:B4, Sigma–Aldrich, St. Louis, MO) 3 days later (9). Prednisolone (PSL, 0.5 mg/kg/day), FTY720 (1 mg/kg/day), or vehicle only was administered every day beginning on day 3. The arthritis scores are shown in the left panel. The *error bars* represent the SEM ($n = 5$ per group). The cancellous bone mineral density (BMD) of the femur was analyzed by pQCT (LCT-200, Aloka, Japan) after killing the mice at day 14. *Error bars* represent the SEM ($n = 5$ per group)

demonstrated that treatment with the S1P receptor agonist FTY720 relieved ovariectomy-induced osteoporosis in mice (a model of postmenopausal osteoporosis in women), by facilitating osteoclast recirculation into blood and reducing the number of mature osteoclasts attached to the bone surface, which suggests a new line of therapy against bone-resorptive disorders [7]. These studies suggest that S1P-targeted therapy would be particularly beneficial for treating RA patients with both immunological and bone-resorptive disorders.

Inspired by this concept, we further examined the therapeutic effect of the S1P receptor agonist FTY720 on simultaneous disease involving both arthritis and osteoporosis (Fig. 1). Ovariectomized mice were injected with an arthrogenic anti-collagen II antibodies cocktail and then with lipopolysaccharide (LPS), so that they developed arthritis in their paws [9]. These mice exhibit both arthritis and osteoporosis and can be regarded as a model of elderly female RA patients. To treat the arthritis, prednisolone (PSL, 0.5 mg/kg/day), FTY720 (1 mg/kg/day), or vehicle only, was administered every day beginning on day 3, and the arthritis score was calculated [10]. We also evaluated bone mineral homeostasis by analyzing the cancellous bone mineral density (BMD) of the femur on day 14. The results showed that the S1P receptor agonist FTY720 was as potent as corticosteroid for suppressing arthritis; in addition, FTY720 recovered the ovariectomy-induced bone density loss, whereas prednisolone did not. As expected, these results clearly suggest that S1P-targeted therapy, such as with S1P receptor agonists, would be beneficial for treating elderly female RA patients who suffer from post-menopausal osteoporosis and arthritis simultaneously.

The effect of S1P receptor agonists is very rapid [4], and robust immunosuppressive effects (by sequestering lymphocytes) can be observed within a few hours after oral administration, although they do not last long (usually disappearing within 12–24 h). Therefore, the profile of an S1P receptor agonist would be similar to that of corticosteroid, rather than to those of methotrexate or other DMARDs. A variety of anticipated S1P-targeted drugs might replace corticosteroids for relieving the inflammation of RA and become a part of the standard RA treatment in the near future. This would be especially conducive to improving the quality of life of elderly patients, who have been left behind so far.

References

1. Van Volenhoven RF (2009) Treatment of rheumatoid arthritis: state of the art 2009. Nat Rev Rheumatol 5:531–541
2. Rosen H, Sphingosine Goetzl EJ (2005) 1-phosphate and its receptors: an autocrine and paracrine network. Nat Rev Immunol 5:560–570
3. Matloubian M, Lo CG, Cinamon G, Lesneski MJ, Xu Y, Brinkmann V et al (2004) Lymphocyte egress from thymus and peripheral lymphoid organs is dependent on S1P receptor 1. Nature 427:355–360
4. Mandala S, Hajdu R, Bergstrom J, Quackenbush E, Xie J, Milligan J et al (2002) Alteration of lymphocyte trafficking by sphingosine-1-phosphate receptor agonists. Science 296:346–349
5. Kappos L, Antel J, Comi G, Montalban X, O'Connor P, Polman CH et al (2006) on behalf of the FTY720 D2201 Study Group. Oral fingolimod (FTY720) for relapsing multiple sclerosis. N Engl J Med 355:1124–1140
6. Japtok L, Kleuser B (2009) The role of sphingosine-1-phosphate receptor modulators in the prevention of transplant rejection, autoimmune diseases. Curr Opin Investig Drugs 10:1183–1194

7. Ishii M, Egen JG, Klauschen F, Meier-Schellersheim M, Saeki Y, Vacher J et al (2009) Sphingosine-1-phosphate mobilizes osteoclast precursors and regulates bone homeostasis. Nature 458:524–528
8. Klauschen F, Ishii M, Qi H, Bajénoff M, Egen JG, Germain RN et al (2009) Quantifying cellular interaction dynamics in 3D fluorescence microscopy data. Nat Protoc 4:1305–1311
9. Terato K, Hasty KA, Reife RA, Cremer MA, Kang AH, Stuart JM (1992) Induction of arthritis with monoclonal antibodies to collagen. J Immunol 148:2103–2108
10. Sasai M, Saeki Y, Ohshima S, Nishioka K, Mima T, Tanaka T et al (1999) Delayed onset and reduced severity of collagen-induced arthritis in interleukin-6-deficient mice. Arthritis Rheum 42:1635–1643

PHILOSOPHICAL TRANSACTIONS OF THE ROYAL SOCIETY A

Phil. Trans. R. Soc. A (2010) **368**, 2983–3000
doi:10.1098/rsta.2010.0093

Cellular modelling: experiments and simulation to develop a physiological model of G-protein control of muscarinic K^+ channels in mammalian atrial cells

BY SHINGO MURAKAMI[1,2,*], SHINGO SUZUKI[1,3], MASARU ISHII[1,4], ATSUSHI INANOBE[1,2] AND YOSHIHISA KURACHI[1,2,*]

[1]*Division of Molecular and Cellular Pharmacology, Department of Pharmacology, Graduate School of Medicine, and* [2]*The Center for Advanced Medical Engineering and Informatics, Osaka University, 2-2 Yamada-oka, Suita, Osaka 565-0871, Japan*

[3]*Graduate School of Engineering Science, Osaka University, 1-3 Machikaneyama-cho, Toyonaka, Osaka 560-0043, Japan*

[4]*Laboratory of Biological Imaging, WPI-Immunology Frontier Research Center, Osaka University, 3-1 Yamada-oka, Suita, Osaka 565-0871, Japan*

The first model of G-protein–K_{ACh} channel interaction was developed 14 years ago and then expanded to include both the receptor–G-protein cycle and G-protein–K_{ACh} channel interaction. The G-protein–K_{ACh} channel interaction used the Monod–Wyman–Changeux allosteric model with the idea that one K_{ACh} channel is composed of four subunits, each of which binds one active G-protein subunit ($G_{\beta\gamma}$). The receptor–G-protein cycle used a previous model to account for the steady-state relationship between K_{ACh} current and intracellular guanosine-5-triphosphate at various extracellular concentrations of acetylcholine (ACh). However, simulations of the activation and deactivation of K_{ACh} current upon ACh application or removal were much slower than experimental results. This clearly indicates some essential elements were absent from the model. We recently found that regulators of G-protein signalling are involved in the control of K_{ACh} channel activity. They are responsible for the voltage-dependent relaxation behaviour of K_{ACh} channels. Based on this finding, we have improved the receptor–G-protein cycle model to reproduce the relaxation behaviour. With this modification, the activation and deactivation of K_{ACh} current in the model are much faster and now fall within physiological ranges.

Keywords: G-protein; GIRK channel; relaxation; heart; atria; computational model

*Authors for correspondence (murakami@pharma2.med.osaka-u.ac.jp; ykurachi@pharma2.med.osaka-u.ac.jp).

One contribution of 13 to a Theme Issue 'The virtual physiological human: computer simulation for integrative biomedicine II'.

1. Introduction

G-protein-coupled receptors (GPCR) make up a large part of the human genome, and they and the G-protein intracellular signalling pathways are involved in the regulation of the cardiovascular system. Defects in the expression and regulation of GPCRs and/or G-proteins underlie various cardiovascular defects and diseases (Smith & Luttrell 2006; Alemany *et al.* 2007), contributing to heart failure (Meij 1996; Feldman *et al.* 2008) and cardiac hypertrophy (Akhter *et al.* 1998; Sakata *et al.* 1998; Barry *et al.* 2008). The G-protein signalling pathways are therefore regarded as therapy targets for cardiovascular diseases and their characteristics need to be understood quantitatively (Alemany *et al.* 2007). Mathematical models of G-protein signalling can play an important role in developing quantitative understanding of these signalling pathways (Thomsen *et al.* 1988; Mackay 1990; Felber *et al.* 1996; Mosser *et al.* 2002; Hao *et al.* 2003; Saucerman *et al.* 2003; Yi *et al.* 2003; Zhong *et al.* 2003; Suh *et al.* 2004; Katanaev & Chornomorets 2007; Linderman 2009). In the heart, models of sympathetic control of voltage-dependent inactivation in the L-type Ca^{2+} channel (Faber & Rudy 2007; Findlay *et al.* 2008) and a biochemical pathway model for β-adrenergic receptor stimulation (Saucerman *et al.* 2003) have been developed. Models of β-adrenergic signalling in the rat ventricular myocyte (Saucerman *et al.* 2003) and modulation of the M-current based upon KCNQ2/KCNQ3 channel subunits expressed in a cell line (Suh *et al.* 2004) were formulated from biochemical assays. To date there have been few models of parasympathetic control (Hosoya *et al.* 1996; Demir *et al.* 1999; Hosoya & Kurachi 1999). In this article, we present the most recent developments of our model of acetylcholine (ACh) activation of cardiac muscarinic K^+ (K_{ACh}) channels. The activation of the K_{ACh} channel is mediated by the βγ subunit ($G_{\beta\gamma}$) of PTX-sensitive G-proteins (G_K) coupled to m_2 or A_1 purinergic receptors in the cardiac cell membrane (Kurachi *et al.* 1986, 1989; Logothetis *et al.* 1987, 1988). Thus, the model is a composite involving the receptor–G-protein cycle and the interaction between the G-protein and K_{ACh} channel.

K_{ACh} channels are activated by intracellular guanosine-5′-triphosphate (GTP_i) in a highly positive cooperative manner at any given concentration of extracellular ACh ($[ACh]_0$) and as the concentration of ACh is increased, both the apparent potency and efficacy of GTP_i are also increased (figure 1*a*,*b*; Kurachi *et al.* 1990; Ito *et al.* 1991). This may reflect properties of the G_K protein–K_{ACh} channel interaction which can be accounted for by the Monod–Wyman–Changeux (MWC) allosteric model with the idea that one K_{ACh} channel is composed of at least four functionally identical subunits, each of which binds one $G_{K\beta\gamma}$ (figure 1*c*; Hosoya *et al.* 1996). For the receptor–G-protein cycle we adopted the model of a receptor-mediated trimeric G-protein reaction cycle developed by Thomsen *et al.* (1988) (figure 1*d*(i)). We combined the two models to construct an integrated model of ACh activation of K_{ACh} channels (Hosoya & Kurachi 1999) which reproduced the steady-state relationship between K_{ACh} channel activity and GTP_i at various $[ACh]_0$ (figure 1*b*).

In isolated atrial myocytes, ACh (0.1 μM) evokes the K_{ACh} current with a half time for activation of 500 ms (Ishii *et al.* 2001). Upon removal of ACh (1.1 μM) from the bath, the current deactivates with a half time of 3.7 s (figure 1*e*; Kurachi *et al.* 1987). The integrated model (Hosoya & Kurachi 1999) could not accurately

reproduce this temporal behaviour of the K_{ACh} current, rather the half time for activation was approximately 1 min and that for deactivation was approximately 2.5 min (figure 1*f*(i, ii); Kurachi & Ishii 2004). Clearly, the model was incomplete.

The K_{ACh} current exhibits strong inward rectification which is caused by Mg^{2+} and polyamines blocking outwardly flowing current. Upon hyperpolarization from a holding potential of -40 mV, the current increases in two distinct phases: instantaneous and slow time-dependent phases. The initial instantaneous increase is due to unblocking of Mg^{2+} and polyamines. The following gradual current increase, which is called 'relaxation', reflects a slow recovery from the reduction of the product of K_{ACh} channel number and K_{ACh} channel open probability (NP_o) that occurs at depolarized potentials. Recently, we have found that regulators of G-protein signalling (RGSs) are involved in this phenomenon (Ishii *et al.* 2001, 2002). RGS proteins stimulate the GTPase activity of the α subunit of G_K proteins ($G_{K\alpha}$) and decrease G_K protein activation (Hepler 1999; Ross & Wilkie 2000). In the resting state this action of an RGS protein is inhibited by the binding of PtdIns(3,4,5)P_3. A Ca^{2+}/calmodulin (CaM) complex, which is formed following depolarization-induced Ca^{2+}-influx across the cardiac cell membrane, displaces PtdIns(3,4,5)P_3 and relieves the inhibition. The activated RGS proteins decrease the activated G_K proteins and thus K_{ACh} channel activity at depolarized potentials. This series of experimental results strongly suggest that relaxation directly reflects G_K protein activity coupling to the K_{ACh} channel. Thus, by analysing the relaxation behaviour of the K_{ACh} current, the physiological kinetics of the receptor-mediated G_K reaction cycle can be obtained. Here we incorporate these ideas into the model of ACh activation of the K_{ACh} channel and we present the model in this paper.

2. Material and methods

(*a*) *Modelling*

The model consists of two parts: an allosteric model representing the interaction between $G_{K\beta\gamma}$ and K_{ACh} channels, and a G-protein cycle model representing the interaction between muscarinic receptors and G_K proteins (figure 1*c*,*d*(ii)). The parameters were searched and verified by comparing the model and experimental results (see §3 and appendix A for details).

(*b*) *Electrophysiological measurements*

Experiments were performed in accordance with the guidelines for the use of laboratory animals of Osaka University. The experimental protocol used here is explained in Ishii *et al.* (2002). In brief, single atrial myocytes were enzymatically isolated from hearts removed from adult male Wister-Kyoto rats. The K_{ACh} currents evoked by various concentrations of ACh were recorded in the whole-cell configuration of the patch-clamp technique. Other experimental data, such as single channel current recording, were taken from published papers (Kurachi *et al.* 1986; Ito *et al.* 1991).

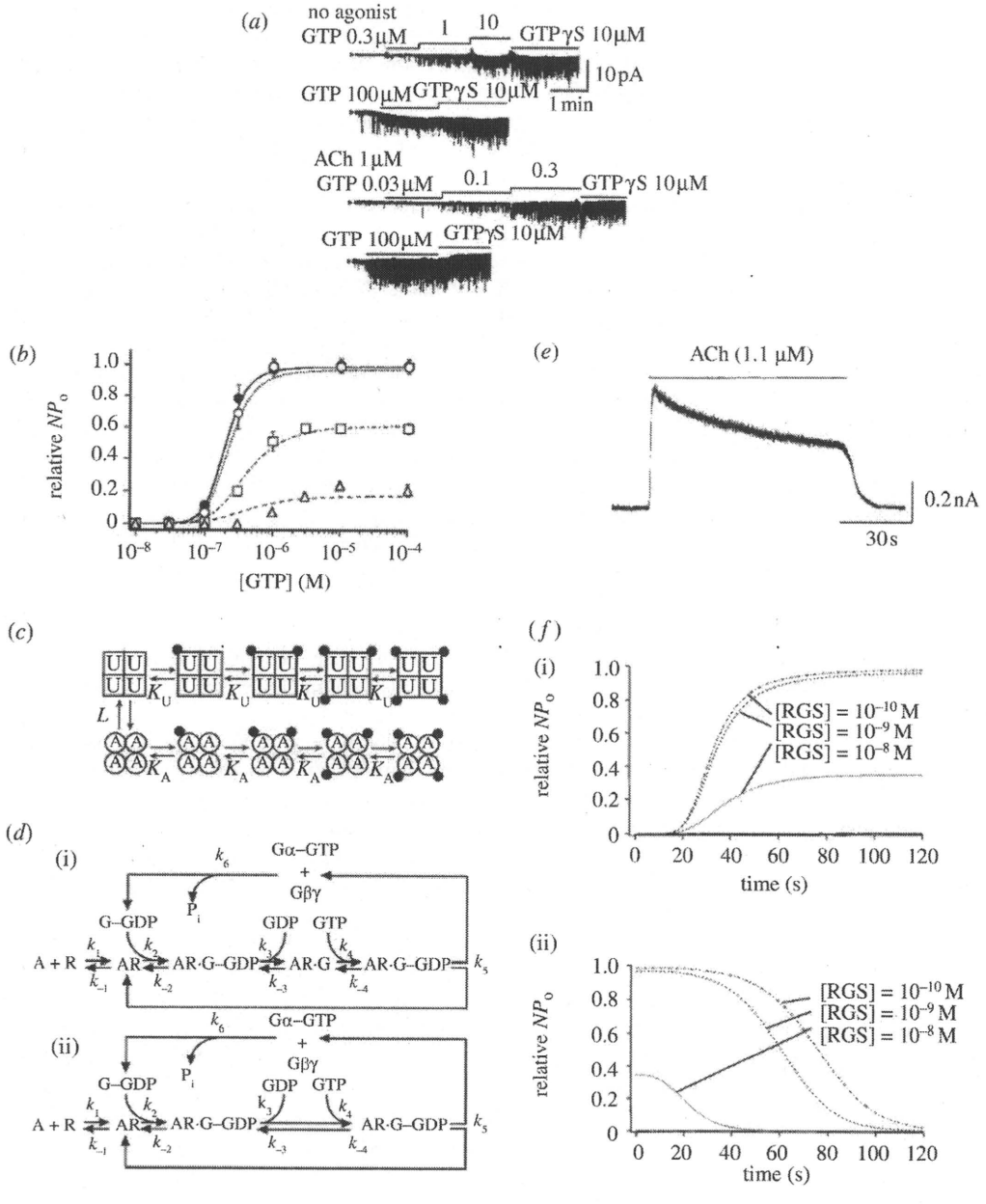

Figure 1. (*Caption opposite.*)

3. Results

(a) *The MWC allosteric model applied to G_K protein–K_{ACh} channel interaction*

Cardiac K_{ACh} channels are activated directly by $G_{\beta\gamma}$ proteins (Logothetis *et al.* 1987, 1988; Kurachi *et al.* 1989). Here, we used the MWC allosteric model (Monod *et al.* 1965) to simulate the interaction between $G_{\beta\gamma}$ and K_{ACh} channels

Figure 1. (*Opposite.*) Previous experimental and simulation studies on K_{ACh} channels. (*a*) Examples of inside-out patch experiments obtained from guinea pig atrial myocytes. The concentration of acetylcholine ([ACh]) in the pipette was 0 or 1 μM as indicated. The bars above each trace indicate the periods of application of the various concentrations of GTP and 10 μM GTPγS to the internal side of the patch membrane. The holding potential was −80 mV. Note that a 3- to 10-fold increase in GTP concentration resulted in a dramatic increase in channel open probability (NP_o) of K_{ACh} channels, indicating the existence of a highly positive cooperative process. (*b*) The experimental relationship between the concentration of GTP and the NP_o of K_{ACh} channels normalized to the maximum NP_o induced by 10 μM GTPγS in each patch (symbols and bars are mean ± s.d.), shown with simulated results obtained with the previous integrated model (Hosoya & Kurachi 1999) of the Monod–Wyman–Changeux (MWC) allosteric model and the Thomsen–Jaquez–Neubig model (lines). [ACh] = 10^{-6} M (filled circles), 10^{-7} M (open circles), 10^{-8} M (squares), 0 M (triangles). (*c*) Schematic of the MWC allosteric model. In this scheme, each K_{ACh} channel is assumed to be an oligomer composed of four identical subunits (i.e. $n = 4$). Each subunit is in either the available (A) or the unavailable (U) state, represented by circles and squares, respectively. Each subunit in the A or U state binds with one dissociated G-protein βγ subunit (filled circles) independently of other subunits, with microscopic dissociation constants K_A or K_U, respectively. In this model, all subunits in the same oligomer must change their conformations simultaneously. Therefore, the channel can be either A_4 or U_4. A_4 and U_4 are in equilibrium through an allosteric constant L. (*d*) Models for receptor–G-protein interaction. (i) Thomsen–Jaquez–Neubig model for receptor–G-protein interaction in the previous model (Hosoya & Kurachi 1999). A, acetylcholine; R, muscarinic m_2-receptor; G, G-protein. (ii) The modified model for receptor–G-protein interaction used in the present study. AR·G is removed and k_6 parameter has been modified. (*e*) The experimental time courses of activation and deactivation phases of 1.1 μM ACh-induced K_G channel currents. (*f*) The simulated time courses of (i) activation and (ii) deactivation phases of 1 μM ACh-induced K_G channel currents in the presence of various concentrations of RGS. The RGS protein action was assumed to be voltage-independent in this prior simulation study (Kurachi & Ishii 2004). RGS accelerated the time course of deactivation but did not affect the activation time course. RGS at high concentrations suppressed maximal channel activity (*a*,*b*). Reproduced and modified from (*a*) Ito *et al.* (1991), (*b*) Hosoya & Kurachi (1999), (*e*) Kurachi *et al.* (1987) and (*f*) Kurachi & Ishii (2004).

in similar ways to Hosoya *et al.* (1996) and Hosoya & Kurachi (1999). In the present study we re-fitted the three parameters of the MWC model to improve the accuracy of the allosteric model. Corey & Clapham (2001) assayed biochemically the profile of $G_{\beta\gamma}$ subunit binding to K_{ACh} channels (GIRK4). They showed that from one to four $G_{\beta\gamma}$ subunits actually bind to one K_{ACh} channel (figure 2*a*, exp.). By comparing the $G_{\beta\gamma}$-binding profile in the actual assay and that estimated by the MWC model, we examined the validity of the parameters that had been used in the previous studies (Hosoya *et al.* 1996; Hosoya & Kurachi 1999; figure 2*a*). The concentration-dependent activation of the K_{ACh} channel by $G_{\beta\gamma}$ and GTP in inside-out patches can be reproduced only with allosteric models (Hosoya *et al.* 1996) and since we now know that a K_{ACh} channel is a tetramer of Kir3.x protein subunits (Corey & Clapham 2001) an allosteric mechanism most probably underlies the activation process. In the MWC model a K_{ACh} channel consists of four protein units (Kir3.x; figure 1*c*). All of the Kir units in a given channel are defined as being in the same state, either tense (T) or relaxed (R), and change their state together (concerted transition). One $G_{\beta\gamma}$

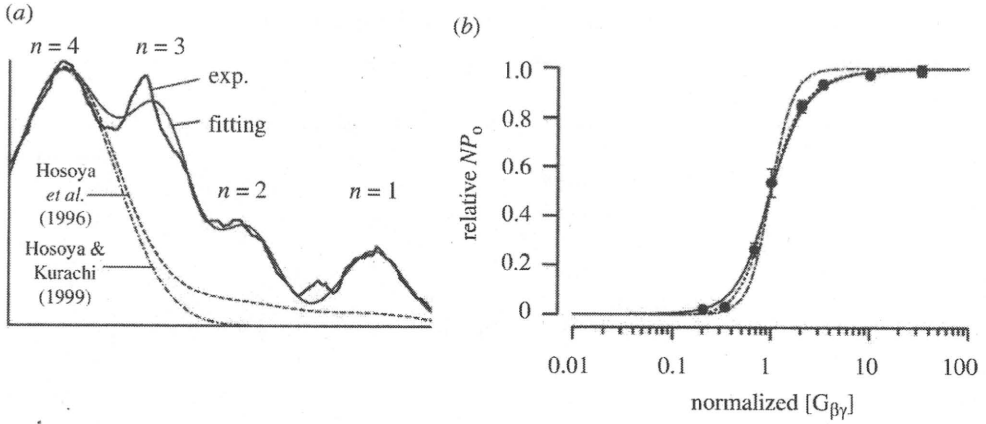

Figure 2. $G_{\beta\gamma}$ protein binding to GIRK channels. (*a*) The densitometry profile of membranes containing GIRK4 with $G_{\beta\gamma}$. Experimental data (exp.) was obtained by densitometry from fig. 3*d* of Corey & Clapham (2001; *n*, the estimated number of $G_{\beta\gamma}$ proteins per channel). Lines represent the densitometry profiles calculated with the parameter sets from the present study (fitting), Hosoya *et al.* (1996) and Hosoya & Kurachi (1999). (*b*) The concentration–response relationship between $G_{\beta\gamma}$ proteins and K_{ACh} channel opening. The fractions of K_{ACh} channels in the open state were calculated with the parameter sets from the present study (solid line), Hosoya *et al.* (1996) (dotted line), and Hosoya & Kurachi (1999) (dot-dash line). Experimental data (circles) from Hosoya *et al.* (1996) were normalized for $G_{\beta\gamma}$ concentration.

protein equilibrates with one Kir protein in either tense or relaxed states with separate equilibrium constants defined as K_T for tense and K_R for relaxed. A tetramer without any $G_{\beta\gamma}$ equilibrates between tense and relaxed states according to the equilibrium constant L. Channels in the relaxed state are considered as available to open with fast gating kinetics (equation (A 1) in appendix A, NP_o), and channels in the tense state are considered to be unavailable (see Hosoya *et al.* 1996 for details).

In the previous studies simulation with the MWC model for G_K–K_{ACh} channel interaction assumed that the majority of the K_{ACh} channels would bind with four $G_{K\beta\gamma}$ subunits, and the numbers of channels binding one, two, or three $G_{K\beta\gamma}$ subunits were practically negligible (figure 2*a*; Hosoya *et al.* 1996; Hosoya & Kurachi 1999). However, the biochemical assay showed that K_{ACh} channels binding one, two, three and four $G_{\beta\gamma}$ represent, respectively, approximately 10, 10, 40 and 40 per cent of the total channel population (figure 2*a*, exp.). Therefore, the parameters used for the MWC model in the previous studies were clearly invalid. In the present study, therefore, the parameters K_T, K_R and L (table 1) were re-calculated with the simplex method to reproduce the densitometry profiles of membranes containing GIRK4 preincubated with $G_{\beta\gamma}$. With the new parameters, the MWC model for the $G_{K\beta\gamma}$–K_{ACh} channel interaction well reproduced the biochemical experimental results (figure 2*a*, fitting).

Figure 2*b* shows the relationships between the K_{ACh} channel NP_o and $[G_{K\beta\gamma}]$ calculated by using the MWC model with the parameter sets used in the previous studies and the present study. The $[G_{K\beta\gamma}]$ values were normalized at the half maximum of the K_{ACh} channel activity. Although L values in the three sets were quite different, all of the relationships exhibited the positive cooperative effect of

Table 1. Parameters of the allosteric and G-protein cycle models.

parameter	value	unit
L	1405	dimensionless
K_R	5.00×10^{-8}	M
K_T	9.09×10^{-7}	M
K_R/K_T	0.0550	dimensionless
k_1	1.67×10^6	$s^{-1}\ M^{-1}$
k_{-1}	0.167	s^{-1}
k_2[G–GDP]	1.80×10^{-2} [G–GDP]	s^{-1}
k_{-2}	0.1	s^{-1}
$k_{3,4}$	2.86×10^3	$s^{-1}\ M^{-1}$
$k_{-4,-3}$[GDP]	6.8×10^{-4}	s^{-1}
k_5	10	s^{-1}
k_6	$1.13\left(1 + \frac{1.30}{1 + \exp(-0.042(V + 25))}\right)$	s^{-1}
$[R]_{total}$	1.87×10^{-3}	M
$[G]_{total}/[R]_{total=}$	30	dimensionless

$[G_{K\beta\gamma}]$ on the K_{ACh} channel NP_o, and the relationship obtained by using the new parameters agrees well with the experimental data. We therefore used the new set of parameters for the MWC model in the following studies.

(*b*) *The G-protein cycle model*

The other part of the ACh activation of cardiac K_{ACh} channel model is the G_K protein cycle which produces $G_{K\beta\gamma}$ subunits. At first, we tested two G-protein cycle models: the Thomsen–Jaquez–Neubig model (Thomsen *et al.* 1988; figure 1*d*(i)) and the Mackay model (Mackay 1990) to see if they could reproduce various characteristics of ACh activation of the K_{ACh} channel. However, after considerable trial and error, we found that neither model was satisfactory when we tried to reproduce at various $[ACh]_0$ not only the steady-state relationship between GTP_i and K_{ACh} channel activity, but also the relationship between the membrane potential and the steady state NP_o of K_{ACh} channels and the voltage-dependent relaxation behaviour. In the present study, we modified the Thomsen–Jaquez–Neubig model. This modified G_K-protein cycle model (figure 1*d*(ii)) is a model of chemical reaction kinetics consisting of concentrations and reaction rate constants (k). AR·G was removed and the k_6 parameter was modified from the original Thomsen–Jaquez–Neubig model. Six values of concentration ([R], [AR], [ARG–GDP], [ARG–GTP], [G–GTP] and [G–GDP] for ACh (A), m_2-receptor (R), G_K protein (G)) in the G-protein cycle model are updated at each calculation step with six ordinary differential equations (equations (A 2)–(A 7) in appendix A). In the previous studies all of the values of rate constants were fixed (figure 1*d*(i)). A novel aspect of the modified model (figure 1*d*(ii)) in the present study is that we have incorporated the concept of regulation of G-protein signalling (RGS). RGS proteins regulate G-protein signalling by accelerating GTP

hydrolysis, and they may be involved in the development of certain cardiovascular pathologies (Wieland & Mittmann 2003; Semplicini *et al.* 2006; Wieland *et al.* 2007; Hendriks-Balk *et al.* 2008). Modulation of GTP hydrolysis by RGS proteins also underlies a voltage- and time-dependent character of the K_{ACh} current in atrial myocytes known as 'relaxation' (figure 3*b*; Inanobe *et al.* 2001; Ishii *et al.* 2001, 2002). Relaxation of the K_{ACh} current reflects an increasing suppression of channel open probability during depolarization and a gradual recovery during hyperpolarization. The time course of these phenomena depends upon voltage-dependent Ca^{2+} influx and Ca^{2+}/CaM modulation of RGS protein activity (Ishii *et al.* 2001). Therefore, GTPase activity of $G_{K\alpha}$ in atrial myocytes can be modulated by RGS proteins in a voltage-dependent manner (Ishii *et al.* 2001). In the modified G_K-cycle model used in the present study, the action of RGS proteins is expressed by the new parameter k_6. The value of each rate constant was fixed, except for k_6 (table 1). Parameter k_6 is defined as a function of membrane voltage so that depolarization of the membrane potential can accelerate GTPase activity (equation (A 8) in appendix A). The rate constants, the total concentration of the receptor ($[R]_{total}$) and a conversion multiplier between inside-out and whole cell recording (r; see §3*a*) were obtained by the simplex method searching for the best fit of the following three properties at various $[ACh]_0$: (i) the steady-state relationships between K_{ACh} channel open probability (NP_o) and GTP_i, (ii) the voltage dependence of K_{ACh} channel NP_o, and (iii) the relaxation time constants at various membrane potentials. We set the value of GTP_i to 100 μM in the whole cell current simulation because this concentration was used in the internal pipette solution in whole cell recording. The $[G_{K\beta\gamma}]$ generated by the G_K protein cycle model was taken into the allosteric model and then the K_{ACh} channel NP_o was calculated by using equation (A 1).

(*c*) *Analysis of simulations with the integrated model*

The improved MWC allosteric model for $G_{K\beta\gamma}$–K_{ACh} channel interaction and the modified G_K protein cycle model were combined into a new integrated model for ACh activation of K_{ACh} channels. The properties of the K_{ACh} current in the integrated model were examined as follows.

(i) *The steady-state relationship between K_{ACh} channel activity and GTP_i*

Since intracellular GTP was not changed in whole cell recording, experimental inside-out patch data for the effect of [GTP] in the presence of different $[ACh]_0$ were taken from Ito *et al.* (1991), converted to that representing whole cell recording and shown as symbols in figure 3*a*. Both GTP and ACh increased K_{ACh} channel activity in a concentration-dependent manner. GTP_i activated the K_{ACh} channel in excised membrane patches much more potently than in whole cell recording. This is probably because in the inside-out patch experiments the internal solution contained high chloride which interferes with the GTPase activity of G_α and increases the sensitivity to GTP by shifting the GTP-relative NP_o curve by 100-fold (Nakajima *et al.* 1992, fig. 4). Therefore, we multiplied the concentration of GTP in excised membrane patch data by 100 to reproduce the GTP_i-dependence of whole cell K_{ACh} currents. Also in the inside-out patch experiments with the high chloride internal solution, GTP_i induced significant K_{ACh} channel activity in the absence of external ACh (figure 3*a*,

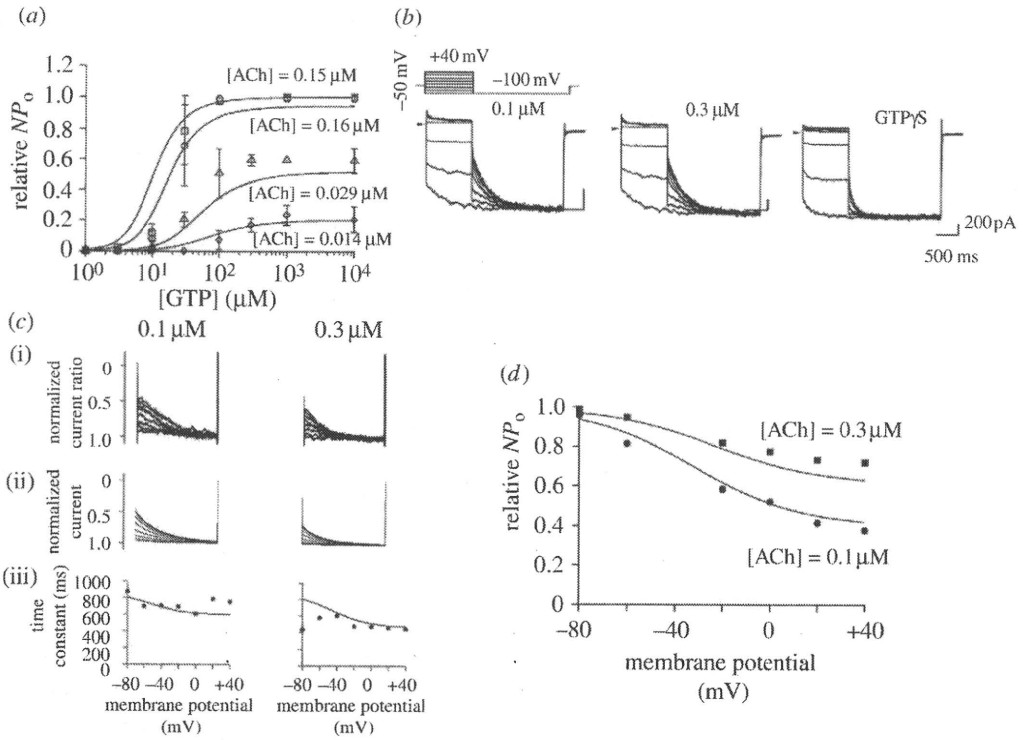

Figure 3. Voltage-dependent relaxation of K_{ACh} current. (*a*) The relationship between K_{ACh} channel open probability (NP_o) and GTP concentration in the presence of different concentrations of ACh. Symbols represent data from Ito *et al.* (1991) and lines represent data obtained from the new model. See text for further details. (*b*) Voltage-clamp single cell current recordings of voltage-dependent relaxation. Single rat atrial cells were subjected to the voltage-clamp protocol inset. Experiments were conducted in the presence of two different concentrations of ACh_0 and 3 μM intracellular GTPγS. (*c*) (i) Normalized K_{ACh} current relaxation traces for 0.1 and 0.3 μM ACh. (ii) Equivalent currents simulated by the model. (iii) Time constants of K_{ACh} current relaxation. Symbols represent experimental data and lines represent the results from model simulation. (*d*) The relationship between the relative K_{ACh} channel availability (NP_o) and prepulse voltage. Experimental data (dots) and simulated results (lines) are shown for ACh concentrations of 0.1 and 0.3 μM.

open diamonds; Nakajima *et al.* 1992, fig. 7). In whole cell recordings there was no detectable K_{ACh} current in the absence of ACh, since in the absence of ACh the G-protein cycle should not be activated at all. Since the basal K_{ACh} current, presumably due to the high chloride, is difficult to separate from the inside-out experimental data, only in this calculation we instead increased the [ACh] in experimental data by an equivalent of 0.01 μM to reproduce the experimental response to GTP in the absence of ACh (figure 3*a*, open diamonds) and then multiplied [ACh] by a fitted parameter of a multiplier r (1.44) to represent a lower sensitivity to ACh in whole cell recording. With these conversions, the model quantitatively reproduced the experimental data for the relationships between K_{ACh} channel activity and GTP_i at various $[ACh]_0$ (figure 3*a*, lines).

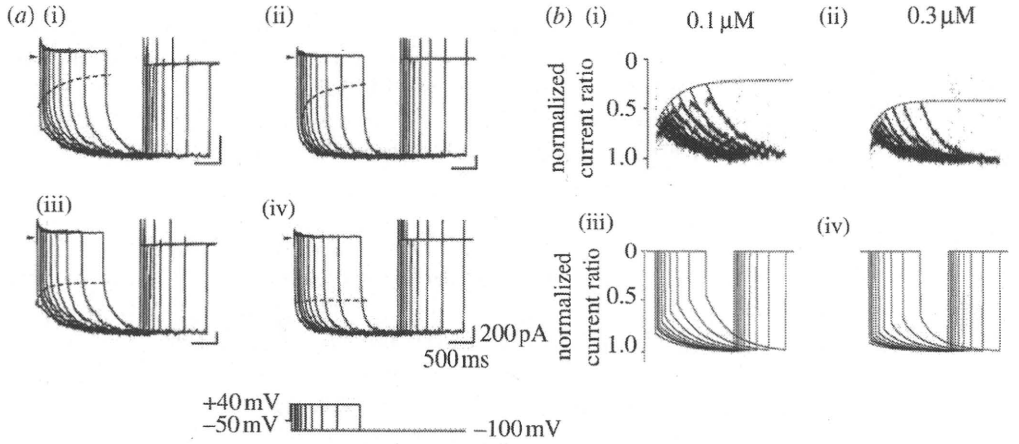

Figure 4. Time-dependent development of K_{ACh} current relaxation. (*a*) Voltage-clamp single cell current recordings from rat atrial cells obtained during a voltage step to −100 mV following a prepulse voltage step to +40 mV of variable duration (22–1306 ms) in cells exposed to either three different concentrations of ACh_0 or 3 μM intracellular GTPγS ((i) 0.1 μM, (ii) 0.3 μM, (iii) 3 μM, (iv) GTPγS). (*b*) (i,ii) Superimposed traces of relaxation currents recorded in the presence of two concentrations of ACh following prepulses of different durations. These currents have been normalized to data recorded in the presence of intracellular GTPγS. (iii,iv) Equivalent currents generated by the model.

(ii) *Voltage and time dependence of the K_{ACh} current*

Voltage- and time-dependent characteristics of the K_{ACh} current are revealed by the phenomenon of relaxation. The experimental relaxation behaviour of K_{ACh} current at various $[ACh]_0$ is shown in figure 3*b*. The preconditioning voltage steps from −100 mV to +40 mV (in 10 mV increments) were applied for 1 s and followed by a test voltage step (2 s in duration) to −100 mV. During the test voltage step relaxation is the slow increase in K_{ACh} current which is observed following a prior instantaneous depolarization (figure 3*b*). This represents the recovery from a time- and voltage-dependent reduction of K_{ACh} current which results from Ca^{2+} entry and Ca^{2+}–CaM stimulation of RGS proteins which accelerate the GTPase activity of the GPCR (Ishii *et al.* 2001, 2002). One characteristic of relaxation is voltage dependence: more of the K_{ACh} current shows relaxation as the prepulse is depolarized. Another characteristic is that relaxation is reduced as $[ACh]_0$ is increased. GTPγS, a non-hydrolysable GTP analogue, also abolished the relaxation behaviour. The time-dependent current change in GTPγS-loaded atrial cells represented the intrinsic gating of K_{ACh} channels.

To extract the character of relaxation, the experimental currents showing relaxation with 0.1 and 0.3 μM ACh were normalized to that evoked by GTPγS (figure 3*c*(i)). The equivalent simulated K_{ACh} currents using the improved integrated model are shown in figure 3*c*(ii). The relaxation is generated by the voltage-dependent facilitation of GTPase activity of $G_{K\alpha}$ due to RGSs. Therefore, we incorporated this process in k_6 of the G_K protein cycle model by formulating k_6 as a function of the membrane potential (table 1, k_6; see §2 for